JACS Au
AN OPEN ACCESS JOURNAL OF THE AMERICAN CHEMICAL SOCIETY

Open Access
This article is licensed under CC-BY-NC-ND 4.0

pubs.acs.org/jacsau
Article

H_2O_2 Triggering Electron-Directed Transfer of Emerging Contaminants over Asymmetric Nano Zinc Oxide Surfaces for Water Self-Purification Expansion

Yingtao Sun, Chun Hu, and Lai Lyu*

Cite This: *JACS Au* 2025, 5, 271−280
Read Online

ACCESS | Metrics & More | Article Recommendations | Supporting Information

ABSTRACT: Slow mass transfer processes between inert emerging contaminants (ECs) and dissolved oxygen (DO) limit natural water self-purification; thus, excessive energy consumption is necessary to achieve ECs removal, which has become a longstanding global challenge. Here, we propose an innovative water self-purification expansion strategy by constructing asymmetric surfaces that could modulate trace H_2O_2 as trigger rather than oxidant to bridge a channel between inert ECs and natural dissolved oxygen, achieved through a dual-reaction-center (DRC) catalyst consisting of Cu/Co lattice-substituted ZnO nanorods *in situ* (CCZO-NRs). During water purification, the bond lengths of emerging contaminants (ECs) adsorbed on the asymmetric surface were stretched, and this stretching was further enhanced by H_2O_2 mediation, resulting in a significant reduction of bond-breaking energy barriers. As a result, the consumption rate of H_2O_2 was reduced by two-thirds in the presence of ECs. In contrast, the removal of ECs was increased approximately 95-fold mediated by trace H_2O_2. It exhibits the highest catalytic performance with the lowest dosage of H_2O_2 among numerous similarly reported systems. This discovery is significant for the development of water self-purification expansion technologies.

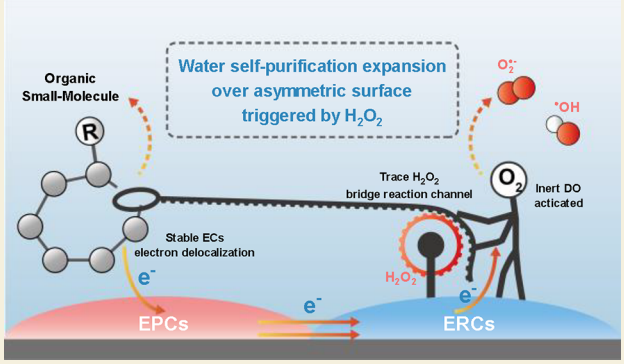

KEYWORDS: *water self-purification expansion, asymmetric surface, trace H_2O_2 trigger, dissolved oxygen reduction, ECs electron delocalization*

INTRODUCTION

The natural water environment is a community of diverse substances coexisting. The realization of its self-purification mainly relies on the natural interaction and mass transfer processes among endogenous coexisting substances such as dissolved oxygen (DO) and pollutants. However, the inertness of endogenous substances and the disorderliness of interaction lead to extremely long natural self-purification periods (Scheme 1a), resulting in increased levels of ECs and pollution of ecosystems,[1−3] which has impeded the United Nations' Sustainable Development Goal of "clean water". Therefore, removing ECs by adding massive oxidants and energy has become a reluctant but forced choice for industry. Heterogeneous advanced oxidation processes (AOPs) have been rapidly developed in water treatment (Fenton-like reaction,[4,5] persulfate activation,[6,7] photocatalysis,[8,9] electrocatalysis,[10−13] etc.) in recent years. Heterogeneous Fenton reaction that generates •OH by adding H_2O_2 (Scheme 1b) has been regarded as an effective water purification process through consuming external energy to enhance mass transfer.[14−19] However, the nonselective redox of H_2O_2 by metal sites[20] on the catalyst surface limited the deep water purification ability of the system under neutral conditions.[21] This limitation was mainly attributable to two key factors: (1) Limited electron transport leads to different rates of metal site cycling during the reaction (Scheme 1a; eqs 1−3). (2) Self-quenching of H_2O_2 with radicals leads to excessive consumption of H_2O_2 (eq 4).

$$M^{n+} + H_2O_2 \rightarrow M^{(n+1)+} + {}^{\bullet}OH + OH^- \quad (1)$$

$$M^{(n+1)+} + H_2O_2 \rightarrow M^{n+} + H^+ + HO_2^{\bullet} \quad (2)$$

$$M^{(n+1)+} + HO_2^{\bullet} \rightarrow M^{n+} + H^+ + O_2 \quad (3)$$

$$H_2O_2 + {}^{\bullet}OH \rightarrow H_2O + HO_2^{\bullet} \quad (4)$$

Received: October 8, 2024
Revised: November 16, 2024
Accepted: December 3, 2024
Published: December 23, 2024

ACS Publications
© 2024 The Authors. Published by American Chemical Society

https://doi.org/10.1021/jacsau.4c00950
JACS Au 2025, 5, 271−280

Scheme 1. Schematic Description of the Reaction Mechanisms of Different ECs Removal Process[a]

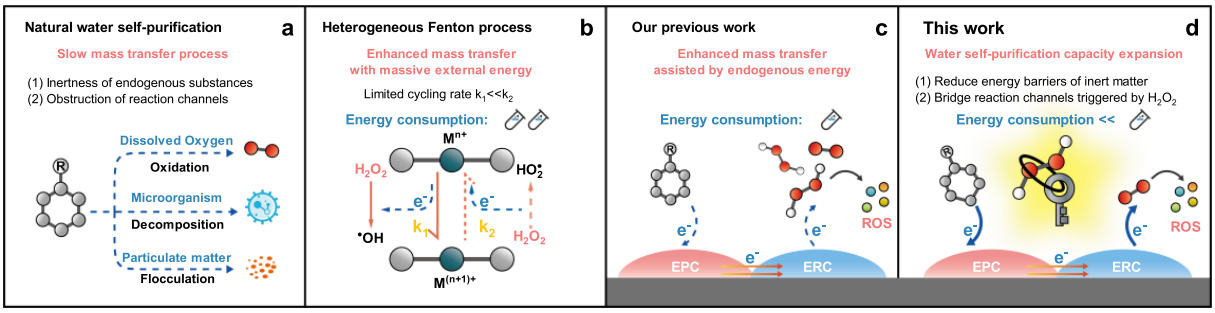

[a](a) Slow water environment self-purification processes. (b) Enhance mass transfer with excess energy consumption in conventional heterogeneous Fenton-like processes. (c) Enhance mass transfer with endogenous energy in DRC catalytic processes. (d) Asymmetric surface expansion of water self-purification capacity triggered by trace H_2O_2.

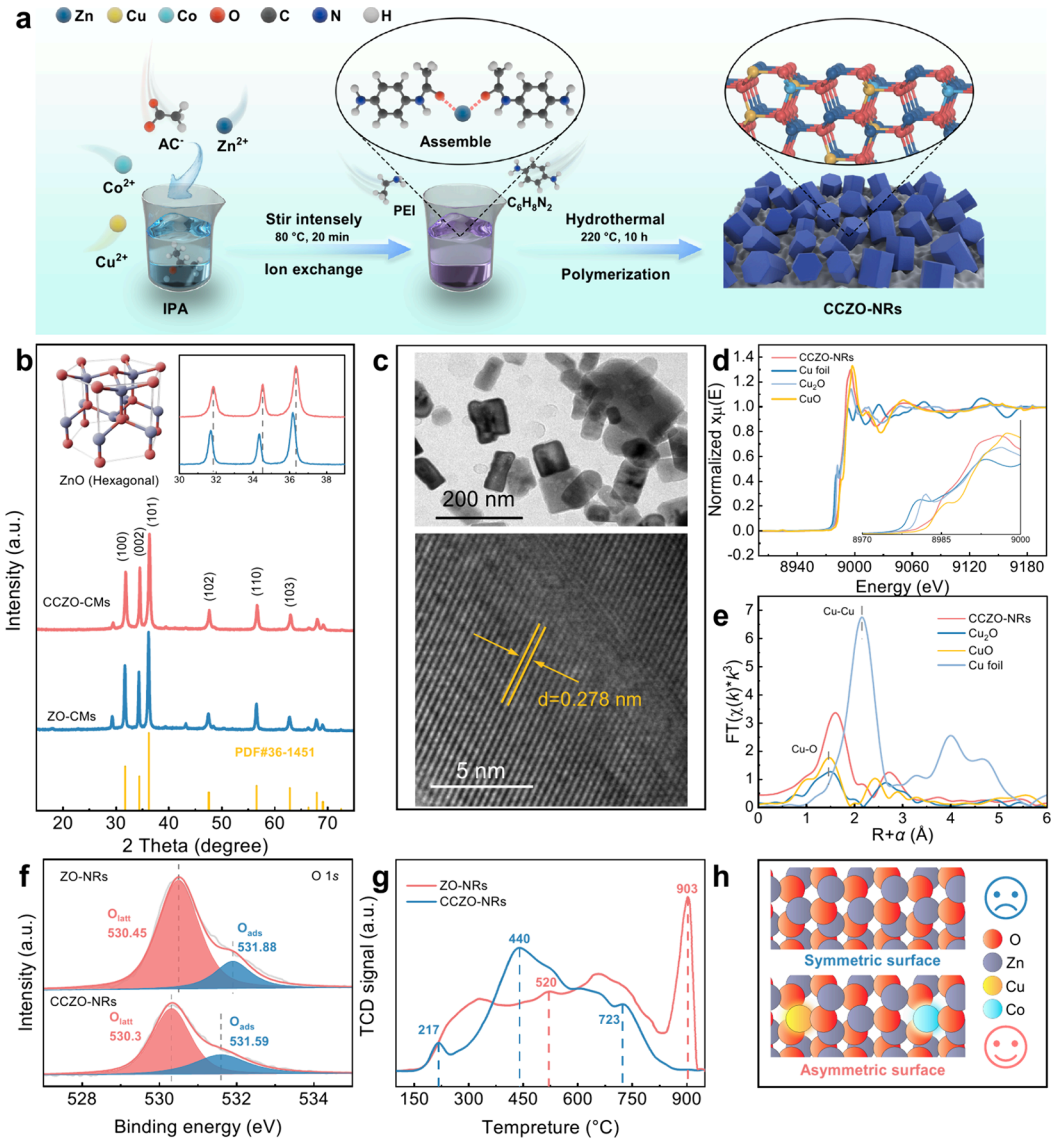

Figure 1. (a) Illustration of the preparation of the CCZO-NRs. (b) Local details of the XRD patterns of CCZO-NRs and ZO-NRs. (c) HRTEM images of CCZO-NRs. (d) Normalized Cu K-edge X-ray absorption near-edge structure (XANES) spectra of CCZO-NRs and reference samples. (e) k^3-weighted Fourier transform extended X-ray absorption fine structure (FT-EXAFS) spectra of CCZO-NRs and reference samples. (f) O 1s XPS spectra of ZO-NRs and CCZO-NRs. (g) shows H_2-TPR curves of the CCZO-NRs and ZO-NRs samples. (h) Illustration of the symmetric surface and asymmetric surface.

https://doi.org/10.1021/jacsau.4c00950
JACS Au 2025, 5, 271−280

To break these limitations, researchers have tried to construct characteristic functional groups, introduce defects/vacancies, modulate the surface electron density on the catalyst surface, etc.[22−24] These methods reduce the reaction energy barriers of inert species in part and accelerate interfacial electron transfer. However, the existing reports seem to neglect the water self-purification process, which is associated with the interaction between natural DOs and ECs on the microsurface. Therefore, expanding the water self-purification capacity by enhancing endogenous substance interactions in water to reduce the energy consumption for ECs removal should be considered.

In fact, most of ECs have aromatic structures with delocalized π-bonds, which are more stable than localized π-bonds and require more energy absorption for bond breakage.[25,26] This is the main reason for the high energy consumption of the conventional process to remove ECs; meanwhile, this is also the main reason for the difficulty of ECs to be removed by water environment self-purification. It is worth noting that the abundant electrons in the delocalized π-bonds are free among the p-orbitals of C atoms.[27,28] These properties could make it possible for catalysts with an asymmetric distribution of surface electrons to in situ directionally modulate the electron distribution of EC-delocalized π-bonds and change the bond lengths of ECs during water purification, which would significantly reduce the bond-breaking energy barrier to expand water self-purification.

Our previous studies[29−31] revealed that the modulation of the electron polarization distribution on the nanocatalyst surface could form electron-rich centers (ERC) and electron-poor centers (EPC) (Scheme 1c), which is aimed at (1) enhancing the activity of Fenton-like reactions by modulating the structure of catalysts to directionally regulate the electron transfer during reaction and (2) reducing H_2O_2 consumption during reaction by utilizing the endogenous substances (DO, ECs, etc.) in wastewater.[32−35] These findings provide the possibility of expanding water self-purification by regulating trace H_2O_2 on microsurfaces to open the reaction channels between ECs and DO.

Herein, a novel asymmetric microsurface DRC catalyst was constructed to modulate H_2O_2 as trigger rather than oxidant at the molecular orbital level during reaction to expand water self-purification capacity. The microsurface was consisted of Cu and Co codoped hexagonal ZnO nanorods (CCZO-NRs), which could in situ modulate the delocalized π−electron directional distribution of ECs to efficiently utilize the energy of endogenous substances in water. Based on the results of experimental characterizations and DFT calculations, the bond lengths of ECs adsorbed on the asymmetric surface were stretched, and this stretching was further enhanced by H_2O_2 mediation, resulting in a significant reduction of bond-breaking energy barriers. The established CCZO-NRs system could efficiently remove different ECs in water with high-efficiency and low-consumption and exhibits the highest catalytic performance with the lowest dosage of H_2O_2 among numerous similar reported systems. Accordingly, it is proposed that the asymmetric surface expansion of water self-purification capacity is triggered by trace H_2O_2 (Scheme 1d). Moreover, the system has excellent performance in adapting to environmental factors and cycling stability, and the biological toxicity of decomposition products is significantly decreased.

RESULTS AND DISCUSSION

Construction and Characterization of CCZO-NRs Asymmetric Surfaces

CuCo-ZnOnps (CCZO-NRs) with an asymmetric surface were synthesized with the assistance of bimetallic metals via ion exchange, in situ assembly, and polymerization steps (Figure 1a). Additionally, Co-ZnOnps (CoZO-NRs), Cu-ZnOnps (CuZO-NRs), and ZnOnps (ZO-NRs) were prepared by controlling the type of metal. X-ray diffraction (XRD) and high-resolution transmission electron microscopy (HRTEM) were initially used to verify the phase structure. As shown in Figure 1b, the XRD pattern of CCZO-NRs exhibited a hexagonal structure of ZnO without the formation of new metal species' characteristic peaks. The 2θ angle of the (101) crystal planes shifted from 36.16 to 36.33° after the codoping of Co and Cu species, which might be attributed to the rearrangement of electrons on the catalyst surface caused by the codoping, hence resulting in a lattice contraction. HRTEM (Figure 1c) confirmed the (100) orientation of the CCZO-NRs.

X-ray photoelectron spectroscopy (XPS) and X-ray absorption near-edge structure (XANES) provide powerful evidence of surface electron rearrangement. The Co and Cu 2p XPS spectra showed the simultaneous presence of multiple valence states (Figure S1a,b), and the Cu K absorption edge energy of CCZO-NRs in XANES (Figures 1d,e) spectra is located between those of Cu_2O and CuO, indicating that the Cu valence is between +1 and +2 caused by the rearrangement of surface electrons due to the introducing metal species. The O 1s XPS spectra (Figure 1f) shows that O_{latt} is shifted to low binding energy after introducing metal species, responding to the significantly altered electronic environment around O after bonding of M (Cu and Co) with O, which provides the possibility for the construction of asymmetric surfaces. Fourier transform extended X-ray absorption fine structure (FT-EXAFS) spectra of CCZO-NRs showed the bonding situation of Cu. Figure S2a,b and Table S1 show the Cu K-edge EXAFS and the curve fit for CCZO-NRs, which exhibit a high fit degree. The first shell of Cu showed a coordination number of about 2 (Cu−O) with a bond length of about 1.59 Å, which is much smaller than the Cu−O bond length of CuO (1.92 Å), confirming that the introduction of Cu species leads to an electronic rearrangement on the lattice rather than forming copper oxide clusters. The WT-EXAFS images (Figures S2 and S3) further corroborate the existence of the main Cu−O and Co−O bonds in CCZO-NRs, which could also prove that Cu/Co atoms have replaced Zn atoms in situ and provide the prerequisites for constructing of asymmetric surfaces.

Furthermore, H_2-TPR technology was used to evaluate the interaction between oxide species and matrix species. Two typical peaks were present in ZO-NRs (Figure 1g), including at 520 °C (reduction of oxygen species) and 903 °C (reduction of zinc oxide species). The peak at 217 °C in the H_2-TPR curves of CCZO-NRs was due to the removal of the adsorbed oxygen species.[36,37] Compared with ZO-NRs, an extremely obvious strong peak located at 440 °C appeared in CCZO-NRs, which was attributed to the reduction of Cu−O−Zn.[38,39] The intensity of the peak located at 723 °C was attributed to the reduction of Co_2O_3 to CoO.[40,41] The lattice substitution of Zn by polymetallics (Cu and Co) in CCZO-NRs also leads to an increased difficulty in the reduction of zinc oxide species, suggesting the strong interactions between Cu/Co and ZnO.

https://doi.org/10.1021/jacsau.4c00950
JACS Au 2025, 5, 271−280

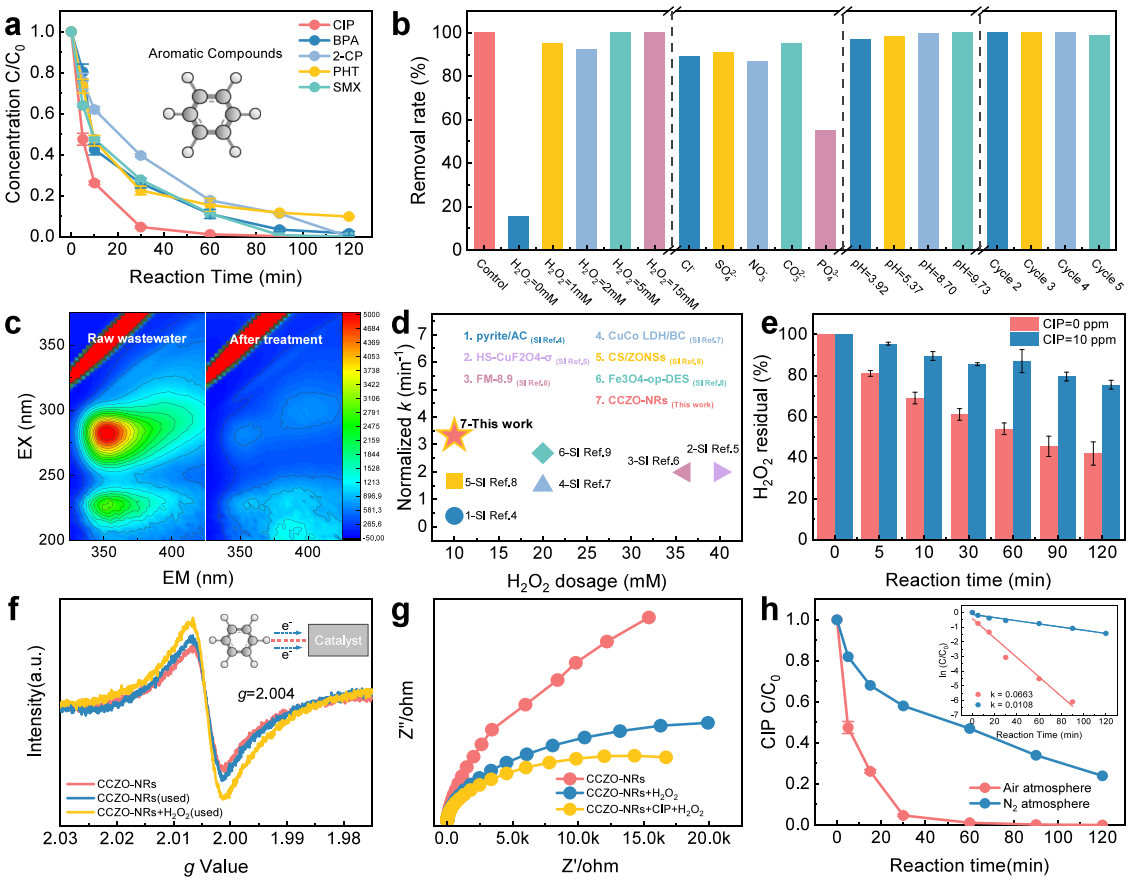

Figure 2. (a) Decomposition curves of different ECs in CCZO-NRs suspensions with H_2O_2. (b) Effect of CIP degradation with different concentrations of H_2O_2, different anions, different pH of initial solution, and the cyclic stability of CCZO-NRs system (detailed experimental steps are shown in Methods). (c) 3D-EEM fluorescence spectra of raw wastewater and the water after 120 min of treatment by the CCZO-NRs system. (d) Comparison of normalized k for CIP removal with those of other reported catalysts. (e) Rate of decomposition of H_2O_2 in different suspensions. (f) EPR spectra of CCZO-NRs before and after reaction in different suspensions. (g) Electrochemical impedance spectroscopy (EIS) Nyquist plots of the CCZO-NR electrode. (h) Degradation rate of CIP by the CCZO-NRs system in different gas atmospheres. The inset shows the pseudo-first-order kinetic rate plots of reaction rate. Reaction conditions: natural pH ∼ 7, initial [pollutant] = 10 mg L^{-1}, initial [H_2O_2] = 10 mM, [catalyst] = 0.2 g L^{-1}, pH adjustment with HCl and NaOH.

Therefore, the bimetallic in situ replacement of Zn atoms in the ZnO substrate results in an asymmetric surface with electron polarization distribution due to the electronegativity difference. Compared to symmetric surfaces with uniform distribution of electrons, asymmetric surfaces contain multiple active sites, which could interact with both electron-rich and electron-poor groups simultaneously (Figure 1h), enhancing microscopic interfacial processes. Strong microinterfacial processes are a prerequisite for expanding the water self-cleaning power.

Water Self-Purification Capacity Expansion Triggered by H_2O_2

The water self-purification expansion performance of CCZO-NRs was evaluated by the degradation of various ECs under natural conditions. As shown in Figure 2a, all selected ECs could be greatly removed within a short amount of time. The oxidative degradation of CIP was selected as the reaction model for subsequent experiments, including ciprofloxacin (CIP), bisphenol A (BPA), 2-chlorophenol (2-CP), phenytoin (PHT), and sulfamethoxazole (SMX). The catalytic performance under various environmental factors and the cycling stability of the catalysts were evaluated with a catalyst dose of 0.2 g L^{-1}, a concentration of CIP of 10 mg L^{-1}, and a concentration of H_2O_2 of 10 mmol L^{-1} as controls. Figure S5 shows the degradation activity of the relevant comparative catalysts, respectively. Obviously, ZnO-NRs lacked the ability in activating H_2O_2. The removal rate of CIP in the suspension of CoZnO-NRs was only about 65% after 120 min. Although CuZnO-NRs had the degradation ability to CIP, the degradation rate was still significantly lower than that of CCZO-NRs. This comparison suggests that polymetallic codoping could further change the structure characteristics of the catalyst surface than single metal doping and greatly enhances the triggering role of H_2O_2 in the pollutant removal process, which was confirmed by DFT calculations of the effect of metal species doping on surface electron density (Figure S6). CCZO-NRs showed excellent catalytic performance at different H_2O_2 concentrations (Figure 2b), even though the concentration of H_2O_2 in the system was only 1 mM, it could still achieve more than 90% removal of CIP. The catalytic performance was not limited by various anions (CO_3^{2-}, Cl^-, PO_4^{3-}, SO_4^{2-}, and NO_3^-) and a very wide pH range (3.8–9.73). Detailed experimental data corresponding to Figure 2b is shown in Figures S7–S9. Furthermore, the change in pH of suspension during the reaction process tended to convert to neutral (Figure S9b) over a wide initial pH range, exhibiting environmentally friendly performance of the catalyst. CIP can

https://doi.org/10.1021/jacsau.4c00950
JACS Au 2025, 5, 271−280

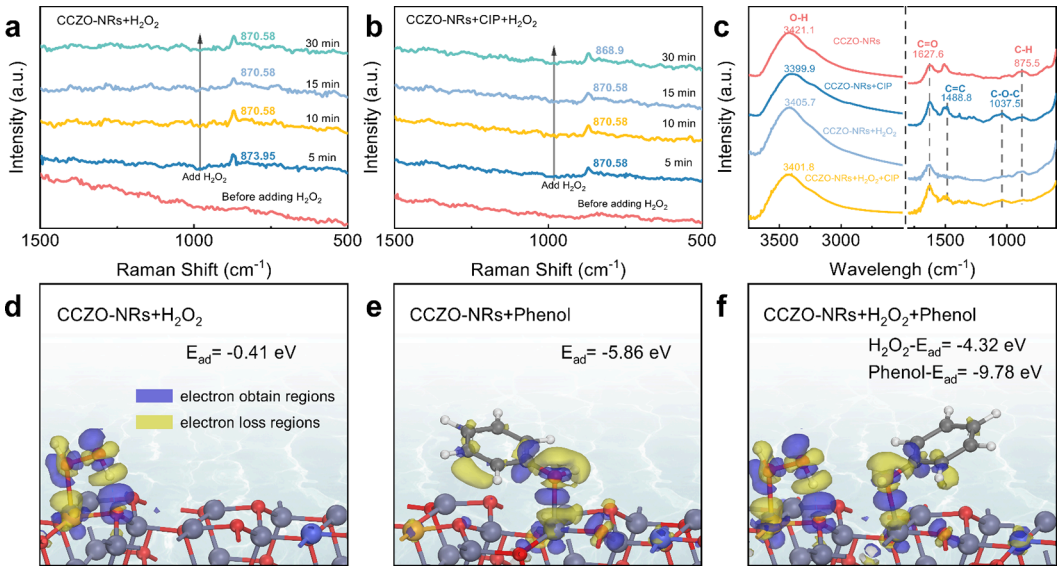

Figure 3. *In situ* Raman spectra in different suspensions. (a) Process of H_2O_2 adsorption by CCZO-NRs and (b) process of CIP degradation reaction with the CCZO-NRs system. (c) FTIR spectra of CCZO-NRs before and after the reaction in different suspensions. The optimized adsorption configurations of (d) H_2O_2 molecules, (e) phenol molecules, and (f) H_2O_2/phenol molecules on the surface of CCZO-NRs.

still be completely removed within 90 min after five cycles, which could also demonstrate the excellent stability and durability of CCZO-NRs.

The purification effect on actual wastewater is an important index for evaluating catalytic performance. Figure 2c shows the degradation of CCZO-NRs on pharmaceutical wastewater (biologically treated wastewater); two main peaks located at 220−230/330−370 nm (peak A) and 275−300/330−370 nm (peak B) were associated with aromatic proteins (such as tyrosine and tryptophan).[42] The intensity of peak A was obviously weakened, and peak B basically disappeared after treatment by the CCZO-NRs system, indicating the potential of CCZO-NRs to be used for industrial wastewater remediation.

In addition, the normalized *k*-values (corresponding equations are shown in Table S2) were calculated for CIP degradation in different catalytic systems (Figure 2d). Notably, the CCZO-NRs exhibited the highest catalytic performance, even with the lowest dosage of H_2O_2. Unexpectedly, H_2O_2 decomposition experiments showed (Figure 2e) that the decomposition efficiency of H_2O_2 was only about 20% during the efficient removal of CIP. On the contrary, the decomposition efficiency of H_2O_2 exceeded 50% in the absence of CIP, which indicated that CCZO-NRs could activate H_2O_2 efficiently, but the efficient removal of CIP seems to be not necessary associated with the activation of H_2O_2, and the presence of CIP inhibited the decomposition of H_2O_2.

To reveal this anomaly, a series of micro-interfacial characterization analyses were performed. Electron paramagnetic resonance (EPR) spectroscopy (Figure 2f) was used to detect unpaired-electron signals on the surface of CCZO-NRs before and after being used. The unpaired electrons of CCZO-NRs increased significantly after adsorbing CIP, suggesting that the electrons of CIP were transferred to the asymmetric surface of the catalyst. The unpaired electrons on the CCZO-NRs surface increased further after co-interacting with H_2O_2 and CIP, suggesting that the presence of H_2O_2 strengthened the electron-donating effect of CIP. Similarly, the charge-transfer resistance on the catalyst surface was measured via electrochemical impedance spectroscopy (EIS) (Figure 2g). The electrode of the system with addition of H_2O_2 and CIP showed a significantly smaller arc radius, which indicated that the involvement of CIP and H_2O_2 resulted in a faster electron transfer rate and a more efficient electron mobility in the system. These findings suggested that the process of EC degradation was accompanied by a high rate of electron transfer between interfaces. Figure 2h shows the degradation rate of CIP by the CCZO-NRs system in different gas atmospheres. There was still 20% of CIP residue after 120 min of reaction in a N_2 atmosphere, and the reaction rate was only 16% of that in an air atmosphere (inset of Figure 2h), which revealed the critical contribution of DO to interface electron transfer and implied the successful expansion of water self-purification.

Water Self-Purification Expansion Mechanisms Triggered by H_2O_2

In situ Raman technology was used to reveal the interfacial reaction process between H_2O_2 and ECs in the CCZO-NRs system. After the addition of H_2O_2 (Figure 3a), a band appeared at 873.95 cm^{-1} attributed to the O−O stretching vibration of H_2O_2 adsorbed on the surface of CCZO-NRs. The peak position shifted significantly to 870.58 cm^{-1} (shift 3.37 cm^{-1}) as the reaction proceeded, indicating a strong interaction of H_2O_2 with CCZO-NRs, which could cause excessive consumption of H_2O_2. The situation changed while adding both CIP and H_2O_2 (Figure 3b), and the peak position changed little as the reaction proceeded (shift is 1.68 cm^{-1}), suggesting that the presence of CIP attenuated the interaction of CCZO-NRs with H_2O_2, allowing H_2O_2 to play the triggering role during CIP degradation. To further elucidate the surface reaction process, CCZO-NRs samples with after different treatments were filtered and dried for FTIR measurement. Previous research has proposed[32,43] that the shift of the ν(OH) groups on the catalyst surface to lower wavenumbers after adsorption of ECs indicates that ECs are deprotonated by electron-directed delocalized via metal complexation on the catalyst surface. ν(OH) groups on

https://doi.org/10.1021/jacsau.4c00950
JACS Au 2025, 5, 271−280

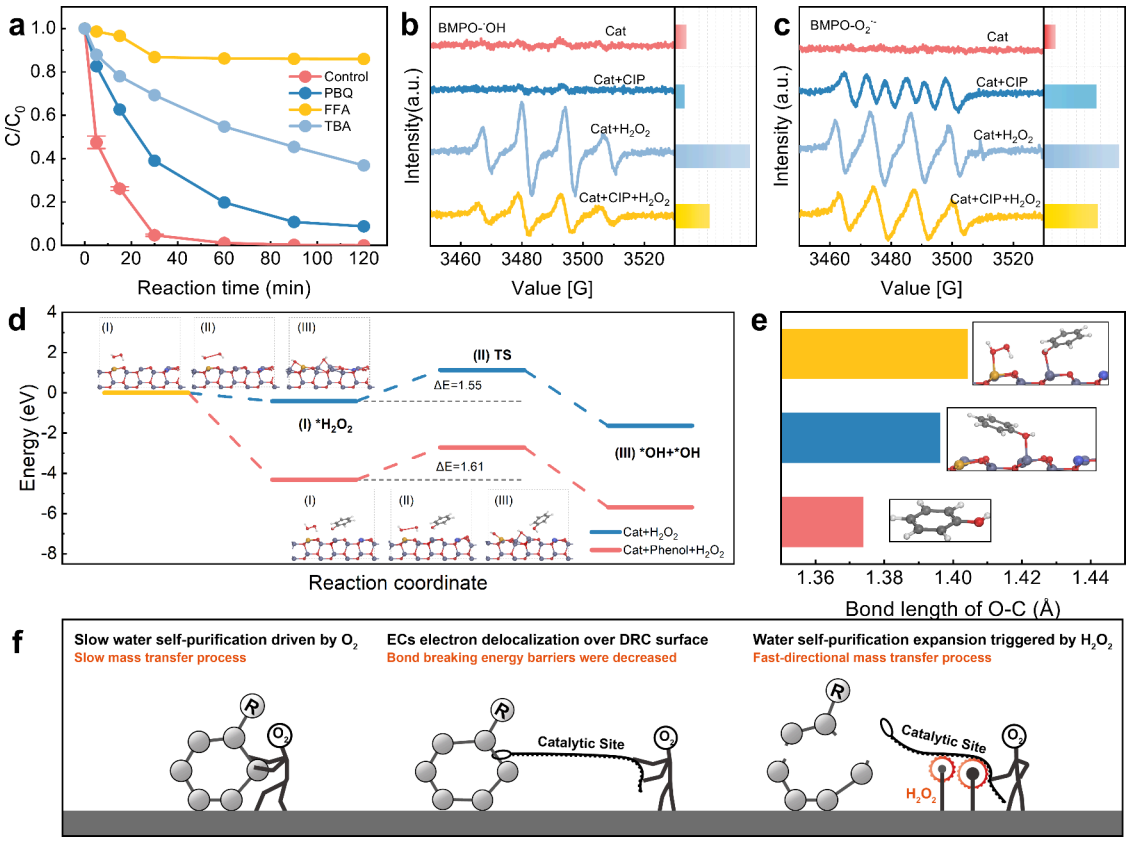

Figure 4. (a) Comparison of removal efficiencies of CIP under different quenchers conditions in CCZO-NRs system; (b) $^{\bullet}OH$ signals and the relative intensity in different suspensions with BMPO. (c) $O_2^{\bullet-}$ signals and the relative intensity in different suspensions with BMPO. (d) Reaction path of H_2O_2 decomposition and free energy profile of $^{\bullet}OH$ production process (inset corresponding intermediate structures). (e) Bond length of phenol (O−C) in different optimized adsorption configurations. (f) Schematic illustration of the mechanism of water self-purification expansion triggered by H_2O_2 at the asymmetric CCZO-NRs surface.

CCZO-NRs (Figure 3c) exhibit a significant wavenumber shift after adsorption of CIP, suggesting that the contaminants complexed with CCZO-NRs by metal species on the surface. Similarly, new bands appeared (Figure 3c) at 1488.8 and 1037.5 cm^{-1} after adsorption of CIP, which were assigned to C═C stretching vibrations and C−O−C stretching vibrations,[44] respectively. The intensities of the C═O stretching vibration and C−O−C stretching vibration peaks were significantly weakened after the addition of H_2O_2, which proved that CIP was adsorbed on the surface of CCZO-NRs, and then led to the chain reaction of CIP degradation by the trigger of trace H_2O_2. To understand the mechanism of interfacial interaction between CIP and asymmetric surface, DFT calculations were performed. Since all ECs contain aromatic structures, the hydroxylated products are inevitably generated during the degradation process; hence, phenol was chosen as the target structure. The best adsorption model (Figures S10 and 3d−f) was obtained through various modeling and calculations (Figure S11). The adsorption energy of H_2O_2 at the Cu site was −0.41 eV (Figure 3d), and that of phenol at the Zn site was −5.86 eV (Figure 3e), indicating that CCZO-NRs have excellent chemisorption activity. Notably, the corresponding adsorption energies of H_2O_2 and phenol increased to −4.32 and −9.78 eV, respectively (Figure 3f), as they were simultaneously adsorbed on CCZO-NRs, indicating that simultaneous action on the catalyst surface could produce stronger interfacial interactions. Projected density of states (PDOS) demonstrates the interaction mechanism of CCZO-NRs with H_2O_2 and phenol at the atomic level. As shown in Figure S12, the Cu 3d peak strongly overlaps with the O 2p peak, indicating that the Cu of CCZO-NRs strongly hybridizes with the O of H_2O_2. Similarly, Zn of CCZO-NRs is strongly hybridized with C of the phenol. These reveal the electron transfer pathway: ECs donate electrons to the Zn sites on the asymmetric surfaces through cation−π interactions, and then to the Cu sites through Zn−O−Cu bond bridges, and finally to H_2O_2 or DO through Cu−O bond bridges.

There remains one more anomaly: The chemisorption becomes stronger, while the consumption of H_2O_2 becomes lower. To reveal this mechanism, radical quenching experiments, EPR measurements, and further DFT were performed. As shown in Figure 4a, after adding TBA ($^{\bullet}OH$ quenching agent), PBQ ($O_2^{\bullet-}$ quenching agent), and FFA ($^1O_2$ quenching agent), the degradation rates of pollutants decreased by ∼60, ∼10, and ∼90%, respectively. Unexpectedly, the addition of the $^1O_2$ quencher greatly inhibited the degradation activity of the catalyst, although there was no significant $^1O_2$ signal detected in the system (Figure S13). This suggests that the efficient removal of ECs in the CCZO-NRs system does not mainly originate from the decomposition of H_2O_2.

On this basis, the activation path of H_2O_2, DO, and H_2O on the catalyst surface during water self-purification was studied by the EPR spin-trap technique with BMPO and TEMP, and the electron transfer processes between the active reaction

https://doi.org/10.1021/jacsau.4c00950
JACS Au 2025, 5, 271−280

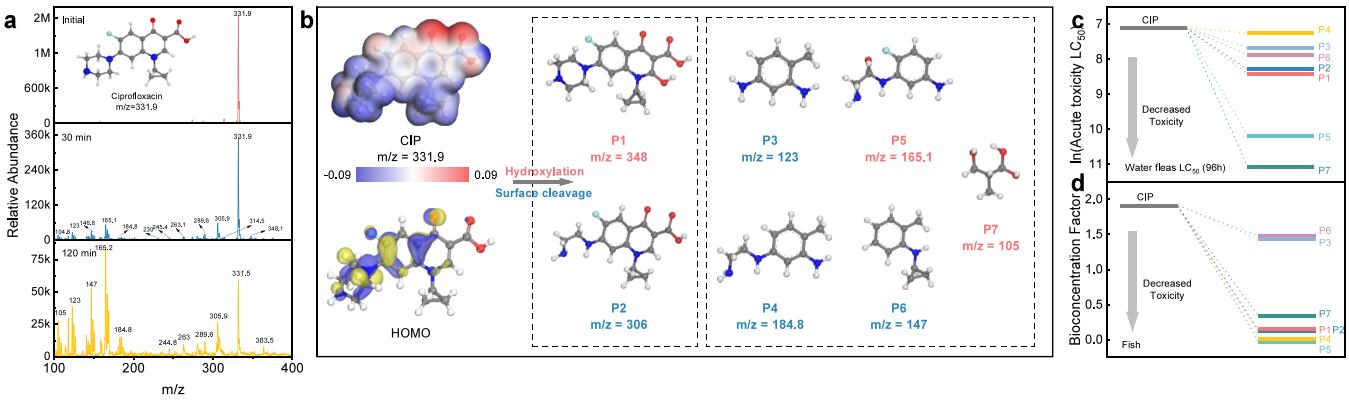

Figure 5. (a) LC-MS spectrum of intermediates during the reaction. (b) Analysis of intermediate products of CIP degradation in the CCZO-NRs/H_2O_2 suspensions by LC-MS (left inset shows the surface electron density and HOMO orbitals of CIP, respectively). Toxicity assessment of degradation products: (c) logarithm of acute toxicity LC_{50} of Daphnia (96h) and (d) bioconcentration factor of fish.

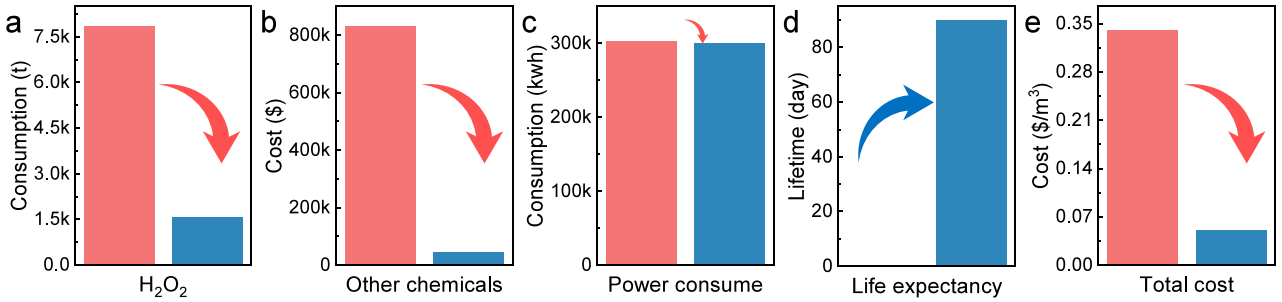

Figure 6. (a) H_2O_2 consumption, (b) cost of other chemicals, (c) power consumed, (d) life expectancy, and (e) total cost comparison of the CCZO-NRs system and conventional Fenton process. The red and blue bars correspond to the conventional Fenton process and CCZO-NRs system, respectively.

centers of CCZO-NRs and solution composition factor were observed simultaneously. In the absence of CIP and H_2O_2, the BMPO-$^{\bullet}$OH (Figure 4b), BMPO-$O_2^{\bullet-}$ (Figure 4c) and TEMP−$^1O_2$ signals (Figure S7) were barely detected in CCZO-NRs system, indicating that there was not enough energy to activate O_2. The situation changed with the addition of CIP to the system, with a quadruple increase in intensity of the BMPO-$O_2^{\bullet-}$ signal (Figure 4c), indicating that enough energy/electron was obtained on CCZO-NRs surface to activate O_2, and this energy could only originate from the CIP without external energy assistance. In the presence of H_2O_2, significant BMPO-$^{\bullet}$OH signal and BMPO-$O_2^{\bullet-}$ signal were detected and the intensities were six times stronger than that in the absence of H_2O_2 (Figure 4b,c), which indicates the excellent activation ability for H_2O_2 over CCZO-NRs. As shown in Figure 4b,c, the BMPO-$^{\bullet}$OH and BMPO-$O_2^{\bullet-}$ signals were evidently weakened in the CCZO-NRs system after adding CIP. Meanwhile, the consumption of H_2O_2 was one-third of that in the absence of CIP (Figure 2e). These further indicated that the efficient removal of ECs did not originate from the decomposition of H_2O_2 but from the mass transfer process between ECs and DO. In this process, CCZO-NRs act as the bridge and H_2O_2 act as the trigger.

Furthermore, the Gibbs free energy of the reaction was calculated to discuss the decomposition of H_2O_2 (one H_2O_2 decomposes into two $^{\bullet}$OH in different systems. Figure 4d illustrates the intermediate structure and corresponding energy distribution. The intermediate state energy barrier for the decomposition of H_2O_2 in the CCZO-NRs/phenol system is significantly higher than that in the CCZO-NRs system, suggesting that H_2O_2 is difficult to decompose in the presence of phenol. On the contrary, calculations of phenol bond lengths show that the O−C bonds of phenol adsorbed on asymmetric surfaces are significantly longer than those of free-state phenol, and the bond lengths are further stretched after introducing H_2O_2, which indicates that the π-electrons in the aromatic structure are delocalized (Figure 4e). These results reveal that (a) CCZO-NRs could directionally shift the electrons of ECs and stretch the bond lengths; (b) trace H_2O_2 could enhance this stretching effect; and (c) the presence of ECs inhibits the decomposition of H_2O_2. These are the key to expanding the water self-purification capacity triggered by trace H_2O_2 for high-efficiency and low-consumption removal of ECs (Figure 4f).

LC-MS technology combined with DFT calculation were used to analyze the decomposition products of CIP for verifying the above interface reaction mechanism (Figure 5a,b). Additional fragments were detected as the reaction proceeded (Figure S9), which included the hydroxylation product and the surface cleavage product of CIP (Figure 5b, surface electron density and HOMO orbitals of CIP demonstrate the potential electron-donating reaction sites). These were the results of ROS (e.g., $^{\bullet}$OH, $O_2^{\bullet-}$, and $^1O_2$) attacking on CIP and electron/energy-donating of CIP, respectively. Combined, the above results indicate that the electron-donating effect of ECs is achieved through the interfacial interaction surface cleavage.

In addition, the biological toxicity of the decomposition products is critical for safe and effective water treatment technologies. Predicted based on the quantitative structure−

https://doi.org/10.1021/jacsau.4c00950
JACS Au 2025, 5, 271−280

activity relationship by the Estimation Programs Interface (EPI) Suite. To ensure the accuracy of the predictions, acute toxicity predictions for Daphnia and bioconcentration factor predictions for fish were performed simultaneously. As shown in Figure 5c,d, compared with CIP, the toxicity of the decomposition products was all decreased; especially the bioconcentration factor was significantly decreased. This indicated that CCZO-NRs could expand water self-purification capacity, besides significantly reducing the toxicity of ECs and eliminating the potential risk of secondary pollution.

Economic Cost–Benefit Evaluation of Self-Purification Expansion Systems

To evaluate the cost-effectiveness of CCZO-NRs during practical applications, an in-depth analysis of the long-term operating costs of the CCZO-NRs system and the conventional Fenton process was performed. As shown in Tables S3 and S4, and Figure 6a–e, the CCZO-NRs system reduces chemical and electricity consumption resulting in a significant reduction of external energy inputs compared with the conventional Fenton process. The whole treatment (Figure 6e) cost (0.05 $/m^3) was only about 1/7 of that of the conventional Fenton (0.34 $/m^3) process for a limited estimated lifetime (90 days). In detail, H_2O_2 consumption of the CCZO-NRs system was reduced to about 1/5 (Figure 6a) and other chemical consumption costs were reduced to about 1/20 (Figure 6b) of that of the conventional Fenton process. Moreover, the lifetime of solid catalysts in long-term operation (Figure 6d) also demonstrated significant advantages (detailed calculations and parameters are shown in Table S4).

CONCLUSIONS

To break through the bottleneck of excessive energy consumption for ECs removal, we propose a mechanism of ECs donating electrons driven by asymmetric surface CCZO-NRs, during which H_2O_2 acts as trigger rather than oxidant to expand the water self-purification effect. Various experiments and DFT calculations confirm that the strong hybridization between 2p orbitals of aromatic C in ECs and 3d orbitals of Zn in CCZO-NRs, combined with the strong polarity of asymmetric surfaces, results in the stretching of the bond lengths of ECs. This stretching was further enhanced by H_2O_2 mediation, resulting in a significant reduction in bond-breaking energy barriers. Notably, the consumption rate of H_2O_2 was reduced by 2/3 in the presence of ECs. In contrast, the removal of ECs was increased approximately 95-fold mediated by trace H_2O_2. It exhibits the highest catalytic performance with the lowest dosage of H_2O_2 among numerous similar reported systems. Long-term operating costs are only about 1/7 of those of conventional Fenton processes. This system also has excellent performance in adapting to environmental factors and cyclic stability, and the biological toxicity of the decomposition products is significantly decreased, which is essential for developing new high-efficiency, low-consumption environmental remediation, and water self-purification expansion technologies.

METHODS

Synthesis of Asymmetric Nano-Surfaces

CCZO-NRs with asymmetric surface was synthesized by a hydrothermal process, and the solution consists of three parts. First, solution of $Zn(CH_3COO)_2$ in 150 mL of isopropanol was heated at 80 °C for 20 min until dissolved to form solution A. Then, a certain amount of $Zn(NO_3)_2{\cdot}6H_2O$, $Cu(NO_3)_2{\cdot}3H_2O$, and $Co(NO_3)_2{\cdot}6H_2O$ was dissolved in solution A. Next, *p*-phenylenediamine and polyethylenimine was dissolved into the mixed solution. Last, the suspension solution was transferred into a Teflon-lined autoclave. The autoclave was placed in a drying oven and kept for 10 h at 220 °C.

Catalytic Performance Evaluation

Generally, 0.01 g of catalyst and 50 mL of CIP solution (10.0 mg L^{-1}) were mixed in a glass beaker and mechanically stirred for 15 min until the adsorption–desorption equilibrium had achieved. Then, the Fenton-like reaction was started with the addition of 50 μL of H_2O_2 (30% w/w) under continuous stirring throughout the experiment (set the temperature at 35 °C). At given time intervals, 1 mL suspensions were collected and filtered by a hydrophobic membrane (pore size 0.22 μm) immediately for detection. Two-time parallel experiments were conducted to calculate error bars.

HPLC Measurements

All of the pollutants were analyzed using a 1200 series HPLC (Agilent, U.S.A.) equipped with a UV detector and a ZORBAX Eclipse XDB-C_{18} column (4.6 × 150 mm, 5 μm). The mobile phase consisted of a 70/30 v/v mixture of methanol/water or 60/40 v/v mixture of acetonitrile/water at a flow rate of 1 mL min^{-1}.

HPLC-MS Analysis

High-performance liquid chromatography–mass spectrometry (HPLC-MS) analysis was conducted in auto full-scan mode (MS). A mixture of (A) water (0.25% formic acid) /(B) methanol was used as the mobile phase. The column temperature was set at 40 °C. The mobile phase procedure followed a gradient elution: 20% B was kept for the first 1 min and then increased to 98% B in 10 min. The flow rate was set at 0.3 mL min^{-1}, and 10 μL of the sample was injected. Mass spectral analysis was conducted in positive mode over a mass range of 50–500 m/z. The cone voltage was 20 V, and the desolvation temperature was 350 °C.

3D-EEM Fluorescence Measurements

In general, 0.01 g of the catalyst powder was first mixed with 50 mL of actual wastewater (35 °C) in an appropriate volume glass beaker. The suspension was stirred for approximately 15 min, and then H_2O_2 (10 mM) was added, triggering reaction. At certain intervals, 3 mL of reaction suspension was collected with a syringe and filtered with a filter (0.45 μm) for follow-up analysis. Three-dimensional excitation emission matrix (3D-EEM) fluorescence spectra of various samples were obtained on an F-7000 spectrometer (HITACHI) with a xenon excitation source, and the slits were set to 5 nm for both excitation and emission. The excitation wavelengths were incremented from 200 to 450 nm in 5 nm steps; for each excitation wavelength, the emission was detected from 300 to 550 nm in 5 nm steps.

Electrochemical Impedance

Electrochemical impedance was measured on an electrochemical workstation (Shanghai Chenhua Instrument Co., Ltd.) equipped with three standard electrodes. The working electrode was prepared from the sample material coated on conductive glass, the reference electrode was extremely saturated calomel, a platinum electrode was used as the pair electrode, and the electrolyte was 0.1 mol/L Na_2SO_4 solution or 10 mg/L CIP prepared with 0.1 mol/L Na_2SO_4.

In Situ Raman and EPR Measurements

In situ Raman spectra for various catalysts were tested with an HR Evolution Raman spectrophotometer (HORIBA Scientific Inc.). The catalyst was placed directly into the reaction cell and scanned from 200 to 2000 cm^{-1} at a resolution of 1 cm^{-1} for 60 s with 40 mW 532 nm laser light irradiation. For the EPR spectral measurement, BMPO/TEMP-trapped EPR signals were detected in different air-saturated methanol/aqueous dispersions of the corresponding samples using a Bruker A300-10/12 EPR spectrometer at room temperature (25–30°). To detect $^{\bullet}OH$, 0.01 g of the prepared powder sample was added to 500 μL of water. Then, 100 μL of the above suspension, 20 μL of BMPO (250 mM), and 50 μL of H_2O_2 (30%, w/w) were mixed thoroughly and then left to stand for 1 min before being drawn into a

https://doi.org/10.1021/jacsau.4c00950
JACS Au 2025, 5, 271–280

capillary for detection. To detect $HO_2^{\bullet}/O_2^{\bullet-}$, the steps were the same as those above except that water was replaced with methanol. To detect $^1O_2$, the steps were the same as that of detecting $^{\bullet}OH$ except that BMPO was replaced with TEMP.

Anion Effect

CO_3^{2-}, Cl^-, PO_4^{3-}, SO_4^{2-}, and NO_3^- correspond to Na_2CO_3, NaCl, NaH_2PO_4, Na_2SO_4, and $NaNO_3$, respectively. 1 mmol L^{-1} of the anion was first dissolved in 50 mL of CIP solution (10 mg L^{-1}) and mechanically stirred until completely dissolved. The subsequent steps are consistent with Catalytic Performance Evaluation.

pH Effect

The pH of the initial CIP solution was adjusted using HCl and NaOH. The subsequent steps are consistent with Catalytic Performance Evaluation.

Cycling Stability Evaluation

After each catalytic performance evaluation, the catalyst was filtered out and dried for the next catalytic performance evaluation, without ever adding a new catalyst (consistently maintaining catalyst the concentration and CIP concentration of 0.2 g L^{-1} and 10 mg L^{-1}, respectively).

Radical Quenching Experiment

Radical quenching experiment was conducted during the CIP degradation experiment. TBA, PBQ, and FFA were used to quench $^{\bullet}OH$, $HO_2^{\bullet}/O_2^{\bullet-}$, and $^1O_2$, respectively. 0.01 g of catalyst and 50 mL of CIP solution (10.0 mg L^{-1}) containing 1 mM quenching agent (TBA, PBQ, and FFA) were mixed in a glass beaker and mechanically stirred for 15 min until the adsorption−desorption equilibrium was achieved. The subsequent steps are consistent with Catalytic Performance Evaluation.

ASSOCIATED CONTENT

Supporting Information

The Supporting Information is available free of charge at https://pubs.acs.org/doi/10.1021/jacsau.4c00950.

Experimental section; figures; and tables (PDF)

AUTHOR INFORMATION

Corresponding Author

Lai Lyu − *Key Laboratory for Water Quality and Conservation of the Pearl River Delta, Ministry of Education, Institute of Environmental Research at Greater Bay, Guangzhou University, Guangzhou 510006, China;* orcid.org/0000-0002-5624-961X; Email: lyulai@gzhu.edu.cn

Authors

Yingtao Sun − *Key Laboratory for Water Quality and Conservation of the Pearl River Delta, Ministry of Education, Institute of Environmental Research at Greater Bay, Guangzhou University, Guangzhou 510006, China*

Chun Hu − *Key Laboratory for Water Quality and Conservation of the Pearl River Delta, Ministry of Education, Institute of Environmental Research at Greater Bay, Guangzhou University, Guangzhou 510006, China*

Complete contact information is available at: https://pubs.acs.org/10.1021/jacsau.4c00950

Notes

The authors declare no competing financial interest.

ACKNOWLEDGMENTS

This work was financially supported by the Key-Area Research and Development Program of Guangdong Province (2023B0101200004), the National Natural Science Foundation of China (52470069, 52122009, and 52350005), the Introduced Innovative R&D Team Project under the "Pearl River Talent Recruitment Program" of Guangdong Province (2019ZT08L387), and the Basic and Applied Basic Research Project of Guangzhou (2024A04J4654, 2024A03J0088).

REFERENCES

(1) Hou, Y.; Liu, F.; Zhang, B.; Tong, M. Thiadiazole-Based Covalent Organic Frameworks with a Donor−Acceptor Structure: Modulating Intermolecular Charge Transfer for Efficient Photocatalytic Degradation of Typical Emerging Contaminants. *Environ. Sci. Technol.* **2022**, *56* (22), 16303−16314.

(2) Tian, C.; Lv, J.; Zhang, W.; Wang, H.; Chao, J.; Chai, L.; Lin, Z. Accelerated Degradation of Microplastics at the Liquid Interface of Ice Crystals in Frozen Aqueous Solutions. *Angew. Chem., Int. Ed.* **2022**, *61* (31), No. e202206947.

(3) Gomes, I. B.; Maillard, J.-Y.; Simões, L. C.; Simões, M. Emerging contaminants affect the microbiome of water systems—strategies for their mitigation. *npj Clean Water* **2020**, *3* (1), 39.

(4) Chen, X.; Fu, W.; Yang, Z.; Yang, Y.; Li, Y.; Huang, H.; Zhang, X.; Pan, B. Enhanced H_2O_2 utilization efficiency in Fenton-like system for degradation of emerging contaminants: Oxygen vacancy-mediated activation of O_2. *Water Res.* **2023**, *230*, No. 119562.

(5) Chen, J.; Qin, C.; Mou, Y.; Cao, Y.; Chen, H.; Yuan, X.; Wang, H. Linker regulation of iron-based MOFs for highly effective Fenton-like degradation of refractory organic contaminants. *Chem. Eng. J.* **2023**, *459*, No. 141588.

(6) Zhao, Z.; Tan, H.; Zhang, P.; Liang, X.; Li, T.; Gao, Y.; Hu, C. Turning the Inert Element Zinc into an Active Single-Atom Catalyst for Efficient Fenton-Like Chemistry. *Angew. Chem., Int. Ed.* **2023**, *62* (18), No. e202219178.

(7) Liu, T.; Xiao, S.; Li, N.; Chen, J.; Zhou, X.; Qian, Y.; Huang, C.-H.; Zhang, Y. Water decontamination via nonradical process by nanoconfined Fenton-like catalysts. *Nat. Commun.* **2023**, *14* (1), 2881.

(8) Zhang, S.; Lan, H.; Cui, Y.; An, X.; Liu, H.; Qu, J. Insight into the Key Role of Cr Intermediates in the Efficient and Simultaneous Degradation of Organic Contaminants and Cr(VI) Reduction via g-C_3N_4-Assisted Photocatalysis. *Environ. Sci. Technol.* **2022**, *56* (6), 3552−3563.

(9) Jiang, Y.; Gao, B.; Wang, Z.; Li, J.; Du, Y.; He, C.; Liu, Y.; Yao, G.; Lai, B. Efficient wastewater disinfection by raised 1O2 yield through enhanced electron transfer and intersystem crossing via photocatalysis of peroxymonosulfate with CuS quantum dots modified MIL-101(Fe). *Water Res.* **2023**, *229*, No. 119489.

(10) Hu, J.; Wang, S.; Yu, J.; Nie, W.; Sun, J.; Wang, S. Duet Fe3C and FeNx Sites for H_2O_2 Generation and Activation toward Enhanced Electro-Fenton Performance in Wastewater Treatment. *Environ. Sci. Technol.* **2021**, *55* (2), 1260−1269.

(11) Qin, X.; Cao, P.; Quan, X.; Zhao, K.; Chen, S.; Yu, H.; Su, Y. Highly Efficient Hydroxyl Radicals Production Boosted by the Atomically Dispersed Fe and Co Sites for Heterogeneous Electro-Fenton Oxidation. *Environ. Sci. Technol.* **2023**, *57* (7), 2907−2917.

(12) Xu, J.; Zheng, X.; Feng, Z.; Lu, Z.; Zhang, Z.; Huang, W.; Li, Y.; Vuckovic, D.; Li, Y.; Dai, S.; Chen, G.; Wang, K.; Wang, H.; Chen, J. K.; Mitch, W.; Cui, Y. Organic wastewater treatment by a single-atom catalyst and electrolytically produced H_2O_2. *Nature Sustainability* **2021**, *4* (3), 233−241.

(13) Dong, C.; Ji, J.; Shen, B.; Xing, M.; Zhang, J. Enhancement of H2O2 Decomposition by the Co-catalytic Effect of WS2 on the Fenton Reaction for the Synchronous Reduction of Cr(VI) and Remediation of Phenol. *Environ. Sci. Technol.* **2018**, *52* (19), 11297−11308.

(14) Peng, J.; Yin, R.; Yang, X.; Shang, C. A Novel UVA/ClO2 Advanced Oxidation Process for the Degradation of Micropollutants in Water. *Environ. Sci. Technol.* **2022**, *56* (2), 1257−1266.
(15) Liang, S.; Zhu, L.; Hua, J.; Duan, W.; Yang, P.-T.; Wang, S.-L.; Wei, C.; Liu, C.; Feng, C. Fe^{2+}/HClO Reaction Produces $FeIVO^{2+}$: An Enhanced Advanced Oxidation Process. *Environ. Sci. Technol.* **2020**, *54* (10), 6406−6414.
(16) Zhang, T.; Huang, C.-H. Modeling the Kinetics of UV/Peracetic Acid Advanced Oxidation Process. *Environ. Sci. Technol.* **2020**, *54* (12), 7579−7590.
(17) Kim, J.; Zhang, T.; Liu, W.; Du, P.; Dobson, J. T.; Huang, C.-H. Advanced Oxidation Process with Peracetic Acid and Fe(II) for Contaminant Degradation. *Environ. Sci. Technol.* **2019**, *53* (22), 13312−13322.
(18) Wei, Z.; Liang, F.; Liu, Y.; Luo, W.; Wang, J.; Yao, W.; Zhu, Y. Photoelectrocatalytic degradation of phenol-containing wastewater by TiO_2/g-C_3N_4 hybrid heterostructure thin film. *Applied Catalysis B Environ.* **2017**, *201*, 600−606.
(19) Lu, C.; Deng, K.; Hu, C.; Lyu, L. Dual-reaction-center catalytic process continues Fenton's story. *Frontiers of Environmental Science & Engineering* **2020**, *14* (5), 82.
(20) Morimoto, Y.; Bunno, S.; Fujieda, N.; Sugimoto, H.; Itoh, S. Direct Hydroxylation of Benzene to Phenol Using Hydrogen Peroxide Catalyzed by Nickel Complexes Supported by Pyridylalkylamine Ligands. *J. Am. Chem. Soc.* **2015**, *137* (18), 5867−5870.
(21) Navalon, S.; de Miguel, M.; Martin, R.; Alvaro, M.; Garcia, H. Enhancement of the Catalytic Activity of Supported Gold Nanoparticles for the Fenton Reaction by Light. *J. Am. Chem. Soc.* **2011**, *133* (7), 2218−2226.
(22) Yang, J.; Zhang, M.; Chen, M.; Zhou, Y.; Zhu, M. Oxygen Vacancies in Piezoelectric ZnO Twin-Mesocrystal to Improve Peroxymonosulfate Utilization Efficiency via Piezo-Activation for Antibiotic Ornidazole Removal. *Adv. Mater.* **2023**, *35* (13), No. e2209885.
(23) Zhang, D.; Li, Y.; Wang, P.; Qu, J.; Li, Y.; Zhan, S. Dynamic active-site induced by host-guest interactions boost the Fenton-like reaction for organic wastewater treatment. *Nat. Commun.* **2023**, *14* (1), 3538.
(24) Xu, X.; Zhang, Y.; Chen, Y.; Liu, C.; Wang, W.; Wang, J.; Huang, H.; Feng, J.; Li, Z.; Zou, Z. Revealing *OOH key intermediates and regulating H_2O_2 photoactivation by surface relaxation of Fenton-like catalysts. *Proc. Natl. Acad. Sci. U. S. A.* **2022**, *119* (36), No. e2205562119.
(25) McGuire, B. A.; Burkhardt, A. M.; Kalenskii, S.; Shingledecker, C. N.; Remijan, A. J.; Herbst, E.; McCarthy, M. C. Detection of the aromatic molecule benzonitrile (c-C_6H_5CN) in the interstellar medium. *Science* **2018**, *359* (6372), 202−205.
(26) Zeng, Z.; Shi, X.; Chi, C.; López Navarrete, J. T.; Casado, J.; Wu, J. Pro-aromatic and anti-aromatic π-conjugated molecules: an irresistible wish to be diradicals. *Chem. Soc. Rev.* **2015**, *44* (18), 6578−6596.
(27) Zhang, G.; Chen, X.-K.; Xiao, J.; Chow, P. C. Y.; Ren, M.; Kupgan, G.; Jiao, X.; Chan, C. C. S.; Du, X.; Xia, R.; Chen, Z.; Yuan, J.; Zhang, Y.; Zhang, S.; Liu, Y.; Zou, Y.; Yan, H.; Wong, K. S.; Coropceanu, V.; Li, N.; Brabec, C. J.; Bredas, J.-L.; Yip, H.-L.; Cao, Y. Delocalization of exciton and electron wavefunction in non-fullerene acceptor molecules enables efficient organic solar cells. *Nat. Commun.* **2020**, *11* (1), 3943.
(28) Liu, Y.; Kilby, P.; Frankcombe, T. J.; Schmidt, T. W. The electronic structure of benzene from a tiling of the correlated 126-dimensional wavefunction. *Nat. Commun.* **2020**, *11* (1), 1210.
(29) Lyu, L.; Zhang, L.; Wang, Q.; Nie, Y.; Hu, C. Enhanced Fenton Catalytic Efficiency of γ-Cu−Al2O3 by σ-Cu^{2+}−Ligand Complexes from Aromatic Pollutant Degradation. *Environ. Sci. Technol.* **2015**, *49* (14), 8639−8647.
(30) Lyu, L.; Yu, G.; Zhang, L.; Hu, C.; Sun, Y. 4-Phenoxyphenol-Functionalized Reduced Graphene Oxide Nanosheets: A Metal-Free Fenton-Like Catalyst for Pollutant Destruction. *Environ. Sci. Technol.* **2018**, *52* (2), 747−756.
(31) Lyu, L.; Yan, D.; Yu, G.; Cao, W.; Hu, C. Efficient Destruction of Pollutants in Water by a Dual-Reaction-Center Fenton-like Process over Carbon Nitride Compounds-Complexed Cu(II)-$CuAlO_2$. *Environ. Sci. Technol.* **2018**, *52* (7), 4294−4304.
(32) Cao, W.; Han, M.; Lyu, L.; Hu, C.; Xiao, F. Efficient Fenton-like Process Induced by Fortified Electron-Rich O Microcenter on the Reduction State Cu-Doped CNO Polymer. *ACS Appl. Mater. Interfaces* **2019**, *11* (18), 16496−16505.
(33) Cao, W.; Luo, Y.; Cai, X.; Wang, S.; Hu, C.; Lyu, L. π-π conjugation driving peroxymonosulfate activation for pollutant elimination over metal-free graphitized polyimide surface. *J. Hazard. Mater.* **2021**, *412*, No. 125191.
(34) Lyu, L.; Lu, C.; Sun, Y.; Cao, W.; Gao, T.; Hu, C. Low consumption Fenton-like water purification through pollutants as electron donors substituting H_2O_2 consumption via twofold cation-π over MoS_2 cross-linking g-C_3N_4 hybrid. *Appl. Catal. B Environ.* **2022**, *320*, 12187.
(35) Deng, K.; Gao, T.; Fang, Q.; Wu, F.; Lu, C.; Zhang, F.; Cao, W.; Han, M.; Hu, C.; Lyu, L. Vanadium tetrasulfide cross-linking graphene-like carbon driving a sustainable electron supply chain from pollutants through the activation of dissolved oxygen and hydrogen peroxide. *Environ. Sci. Nano* **2021**, *8* (1), 86−96.
(36) Zhang, H.; Li, C.; Lyu, L.; Hu, C. Surface oxygen vacancy inducing peroxymonosulfate activation through electron donation of pollutants over cobalt-zinc ferrite for water purification. *Applied Catalysis B Environ.* **2020**, *270*, No. 118874.
(37) Zhong, S.; Sun, Y.; Xin, H.; Yang, C.; Chen, L.; Li, X. NO oxidation over Ni−Co perovskite catalysts. *Chemical Engineering Journal* **2015**, *275*, 351−356.
(38) Polnišer, R.; Štolcová, M.; Hronec, M.; Mikula, M. Structure and reactivity of copper iron pyrophosphate catalysts for selective oxidation of methane to formaldehyde and methanol. *Applied Catalysis A: General* **2011**, *400* (1−2), 122−130.
(39) Zhou, X.; Jawad, A.; Luo, M.; Luo, C.; Zhang, T.; Wang, H.; Wang, J.; Wang, S.; Chen, Z.; Chen, Z. Regulating activation pathway of Cu/persulfate through the incorporation of unreducible metal oxides: Pivotal role of surface oxygen vacancies. *Applied Catalysis B Environ.* **2021**, *286*, No. 119914.
(40) Zhan, S.; Zhang, H.; Mi, X.; Zhao, Y.; Hu, C.; Lyu, L. Efficient Fenton-like Process for Pollutant Removal in Electron-Rich/Poor Reaction Sites Induced by Surface Oxygen Vacancy over Cobalt-Zinc Oxides. *Environ. Sci. Technol.* **2020**, *54* (13), 8333−8343.
(41) Li, Z.; Meng, M.; Zha, Y.; Dai, F.; Hu, T.; Xie, Y.; Zhang, J. Highly efficient multifunctional dually-substituted perovskite catalysts $La_1-xK_xCo_{1-y}Cu_yO_{3-\delta}$ used for soot combustion, NO_x storage and simultaneous NOx-soot removal. *Applied Catalysis B Environ.* **2012**, *121−122*, 65−74.
(42) Cui, Y.; Wu, Q.; Yang, M.; Cui, F. Three-dimensional excitation-emission matrix fluorescence spectroscopy and fractions of dissolved organic matter change in landfill leachate by biological treatment. *Environ. Sci. Pollut Res. Int.* **2016**, *23* (1), 793−799.
(43) Sun, Y.; Hu, C.; Lyu, L. New sustainable utilization approach of livestock manure: Conversion to dual-reaction-center Fenton-like catalyst for water purification. *npj Clean Water* **2022**, *5* (1), 53.
(44) Wang, Y.; Zhang, P.; Lyu, L.; Liao, W.; Hu, C. Efficient destruction of humic acid with a self-purification process in an Fe^0-Fe_yC_z/Fe_x-GZIF-8-rGO aqueous suspension. *Chem. Eng. J.* **2022**, *446*, No. 136625.

https://doi.org/10.1021/jacsau.4c00950
JACS Au 2025, 5, 271−280